ORIGINAL ARTICLE

Tool path planning for five-axis U-pass milling of an impeller

Jingyang Feng[1] · Zhaocheng Wei[1] · Minjie Wang[1] · Xueqin Wang[1] · Minglong Guo[1]

Abstract

U-pass milling is a roughing method that combines the characteristics of flank milling with conventional trochoidal milling. The tool cuts in and out steadily, and the tool–workpiece wrap angle is maintained within a small range. This method can smooth the cutting force and reduce the peak cutting force while avoiding cutting heat accumulation, which can significantly improve the processing efficiency and reduce tool wear. In this study, a tool path model is established for U-pass milling, and the characteristic parameters of the path are defined. Through a comparative test of three-axis groove milling, it is demonstrated that the peak value and average value of the cutting force are reduced by 25% and 60%, respectively. An impeller runner is considered as the processing object, and the milling boundary parameters are pretreated. A tiling micro-arc mapping algorithm is proposed, which maps the three-dimensional boundary to the two-dimensional parameter domain plane with the arc length as the coordinate axis, and the dimensionally reduced tool contact point distribution form is obtained. The geometric domain tool position point and the interference-free tool axis vector are obtained by calculating the bidirectional proportional domain of the runner and the inverse mapping of any vector in the parameter domain. Finally, the calculation results are nested into the automatically programmed tool (APT) encoding form, and the feasibility of the five-axis U-pass milling tool path planning method is verified through a numerical example.

Keywords U-pass milling, · Cutting force, · Dimensionality reduction mapping, · Tool position point, · Tool axis vector, · APT code

1 Introduction

Integral impellers are widely used in the aerospace, energy, and power fields. With the rapid development of industrial technology, demand has increased sharply, and higher integral impellers are widely used in the aerospace, energy, and power fields. With the rapid development of industrial technology, demand has increased sharply, and higher requirements for the processing cost and efficiency of the product have been put forward [1–3]. Approximately 70–90% of the machining allowance in impeller molding is removed through rough machining. For example, in the McDonnell Douglas DC-10 aircraft, there are 16 different alloy impellers in the CF6-50 engine produced by General Electric. The total mass of the blank can be as high as 3311 kg, but the mass after forming is only 381 kg, representing a removal of approximately 88% [4, 5]. Improving the processing efficiency of such parts is an important research direction under the current background of highly energy-efficient processing.

For integral impeller machining, the conventional 3+2 layer milling [6–8] tool path plan is simple and widely used. However, in actual machining, the tool tip is usually the main cutting area, which leads to rapid tool wear and a short tool life. In addition, the conventional linear layer-by-layer tool path usually has a large number of redundant tool paths and a low material removal rate. These problems lead to long processing cycles and high production costs, especially in cavity machining processes with large material removal. To achieve high-efficiency machining of deep cavities with large material removal, plunge milling has been widely used as an intermittent milling method [9–11]. This is a fundamentally different process from conventional layer milling. The cutting process is completed by up and down movements of the tool along the Z-direction. It is characterized by good process stability, and the cutting force is mainly along the tool axis with greater rigidity. Plunge milling is divided into wall plunge

✉ Zhaocheng Wei
   wei_zhaocheng@dlut.edu.cn

1 Key Laboratory for Precision and Non-traditional Machining Technology of Ministry of Education, Dalian University of Technology, Dalian, People's Republic of China 116024

milling and groove plunge milling according to the different processing objects. The former is suitable for highly perpendicular sidewall finishing [12], whereas the latter can realize high-efficiency rough machining of deep cavity structures [13, 14]. The efficiency of plunge milling is significantly higher for machine tools with higher rigidity and acceleration than layer milling [15]. For impeller runners with large diameters, widths, and depths, the plunge milling method can operate with higher efficiency by removing a large amount of material through a single pass. However, for a wall structure with a large inclination angle, the remaining material for plunge milling is large and uneven. At the same time, when facing a flat impeller with a medium runner depth, the residual amount at the bottom after a single plunge milling is large, which often requires secondary machining and affects the machining efficiency.

Flank milling [16, 17] is a common processing method for ruled-surface blades. During the cutting process, the side edge of the tool is always in contact with the processed surface, and the envelope surface formed by the blade generatrix during processing is used to approximate the curved surface. The current research has established mature theories related to flank milling in terms of ruled-surface tool path planning, tool axis vector calculation, and compensation estimation [18–20]. Because the flank milling method uses a larger axial cutting depth, it can greatly reduce the number of layer-by-layer passes, and the conical milling cutter can better ensure the blade machining accuracy. Compared with the layer milling method, the flank milling method is generally used for finishing or semi-finishing.

The tool path of trochoidal milling, which is composed of a uniform circular arc and linear interpolation, differs from the above methods. Initially, Elber [21] proposed and planned a tool path adapted to a narrow runner, solved the problem of redundant and discontinuous tool paths caused by the linear cutting form, and established the effectiveness of this method. Subsequently, the standard circle model, cycloid circle model, and variable radius cycloid circle model were proposed and have been widely used [22–24]. A large number of contrast tests have demonstrated that the smooth cutting-in and cutting-out method can effectively avoid load mutations during the milling process, smooth the cutting force, reduce the peak cutting force, and avoid full-edge cutting. During the entire machining cycle, the tool–workpiece wrap angle is within a small range, and the time when the tool is actually in the cutting area during a rotation cycle is short; at the same time, the tool is not always in the cutting state during a trochoidal cutting cycle. This type of cutting can quickly dissipate the cutting heat and avoid severe tool wear caused by local temperature surges [25–28]. However, most of the current research still plans trochoidal passes based on the layer milling method, which is essentially the same as conventional layer milling. When the blank depth is large, the tool still needs to reciprocate layer-by-layer, and the problem of severe tool wear caused by a processing mode with the tool tip point as the main cutting area remains. When facing a groove with a large width, multiple reciprocating machining is usually required, the reserved area of the initial feed is long, and the machining allowance is large; thus, the efficiency is not significantly improved in the actual processing. Subsequently, Kamil [29] established a trochoidal milling tool path based on flank milling by increasing the axial cutting depth. The influence of different tools and different trochoidal trajectories on the surface roughness and chipping were analyzed, and the efficient machining of deep grooves was realized. Nam-Seok [30] combined the characteristics of flank milling to apply trochoidal milling to titanium alloy processing. Tests showed that compared with the layer milling method, the specific cutting energy was decreased, while the cutting force was significantly reduced, demonstrating the high efficiency of this combination method.

Different tool path forms are shown in Fig. 1. In summary, for rough machining of large-depth blanks, the combination of flank milling and trochoidal milling can effectively improve the processing efficiency. U-pass milling is a tool path strategy based on trochoidal milling combined with the characteristics of flank milling, as shown in Fig. 2. It can be seen from the geometric form that this method combines the characteristics of smooth cutting-in and cutting-out of layered trochoidal milling with the large axial depth and high processing efficiency of flank milling. However, research on tool path planning for U-pass milling has not yet been reported.

Therefore, in this study, a tool path model for U-pass milling is established, the characterization parameters of the path are defined, and the advantages of this milling method are verified through three-axis milling tests. Taking an impeller runner as the processing object, a pretreatment method for the milling boundary is established. A mapping algorithm for tiling micro-arcs is proposed that maps the three-dimensional boundary to the two-dimensional parametric domain plane with the arc length as the coordinate axis and calculates the tool contact points in different cycloid areas based on the boundary with reduced dimensionality. By calculating the bidirectional proportional domain of the runner and the inverse mapping of any vector in the parameter domain, the geometric domain tool position point and the interference-free tool axis vector are obtained. Finally, the calculation results are nested into the automatically programmed tool (APT) encoding form, and the feasibility of the five-axis U-pass milling tool path planning method is verified through a numerical example. The structure flow is shown in Fig. 3.
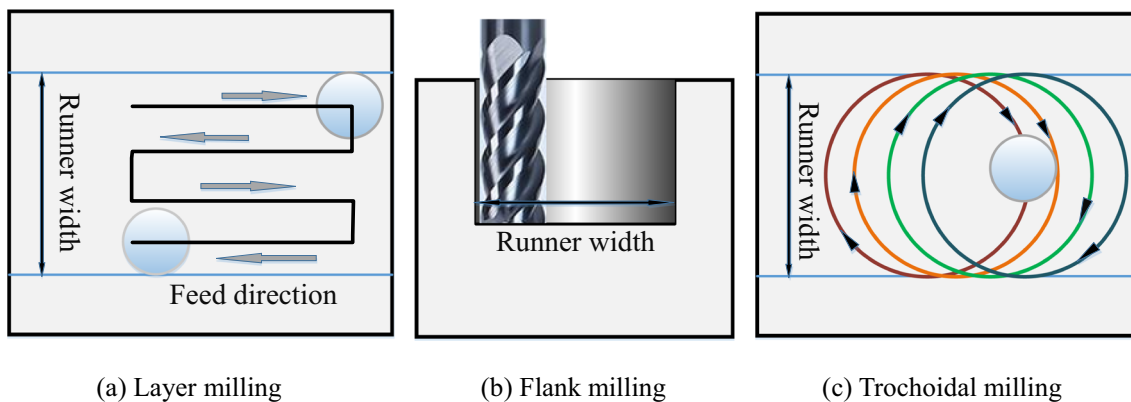
(a) Layer milling   (b) Flank milling   (c) Trochoidal milling

Fig. 1 Tool paths. (a) Layer milling. (b) Flank milling. (c) Trochoidal milling

2 U-pass milling model and comparison tests

2.1 U-pass geometry model

The single-cycle U-pass milling tool path is composed of four basic areas, and the corresponding parts are defined as the cycloid area (left and right cycloid circles), step connection area, and transition area, as shown in Fig. 4. The initial point of tool cutting-in is O_{st}. In the left cycloid circle area, the tool is always tangent to the runner boundary, N_{left}. At this time, the tool–workpiece wrap angle changes continuously within a small range. When the tool is tangent to L_{st}, it enters the stepping connection area. In the current range, the tool always cuts with a constant tool–workpiece angle, and the cutting thickness remains unchanged. After leaving the step connection area, the tool enters the symmetrical right cycloid circle to continue cutting. The cutting form is the same as that of the left cycloid circle area. Then, the tool cuts away from the (n)th cycle and transits through the transition area to the initial point of the (n+1)th cycle, $O_{st,n+1}$, to complete the single-cycle U-pass milling.

The path parameters of U-pass milling are different from those of linear and arc milling. U-pass milling involves multiple characterization parameters: a. the cycloid position angle, τ (°), is the relative angle of the tool position to the center of the cycloid circle in this cycle; b. the cycloid circle radius, R_{cy} (mm), is the radius of the revolution circle of the tool around

the center of the cycloid circle; c. the cycloid step f_{cy} (mm), is the span length of two U-pass cycles and is equal to the distance between the centers of the two cycles, with a direction perpendicular to the step connection line and pointing from the (n)th to (n+1)th cycle; and d. the cycloid feed speed, f (mm/min), is different from linear milling. The feed direction corresponding to different position angles, τ, in the cycloid area is always along the direction tangent to the current cycloid circle.

2.2 Test comparison

The machine code is established based on the above milling model. The cutting force distributions of conventional milling methods and U-pass milling are compared using groove milling tests. The machining model is shown in Fig. 5.

The cutting force is measured using a YDCB-III05 three-way piezoelectric quartz dynamometer, and the machining entities with different tool paths are shown in Fig. 6.

Under the same feed per tooth, f_z, and material removal rate, MRR, conditions, the cutting forces of U-pass milling and conventional milling are compared. The U-pass milling combined with the characteristics of flank milling can complete the processing with a small wrap angle, cut in and cut out smoothly, and allow larger axial cutting depth. In order to ensure the same parameters, the conventional layer milling must choose a large step length. If the axial cutting depth
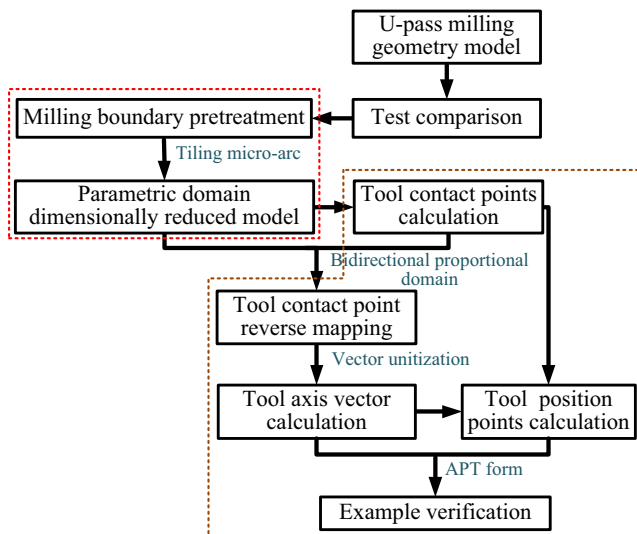
Fig. 2 U-pass milling
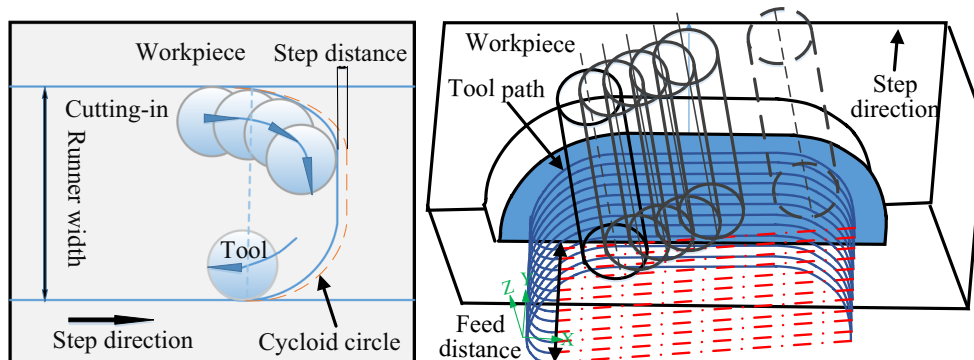
Fig. 3 Overall structure flow chart

Fig. 5 Machining model

increases at the same time, the cutting load will increase rapidly, and the tool is prone to fracture, so it is not suitable for processing. In the contrast test, the axial cutting depth of the former is four times that of the latter. The three-dimensional cutting force is obtained through signal acquisition, and the results of the tests are summarized in Table 1.

The collected data are processed using MATLAB software. The distribution of the cutting force under processing conditions of $MRR = 2$ cm^3/min and $f_z = 0.04$ mm/min is shown in Fig. 7, where (a) represents the component force in the x-direction, (b) and (c) represent the cutting component forces in the y-direction and z-direction, respectively, and (d) represents the resultant cutting force, F_{res}, as shown in Eq. 1.

$$F_{res} = \sqrt{F_x{}^2 + F_y{}^2 + F_z{}^2} \tag{1}$$

It can be seen in the Fig. 7 that the absolute value of the three-dimensional cutting force in the cycloid region initially increases and then decreases. This is mainly because the tool–workpiece wrap angle at this stage initially increases and then
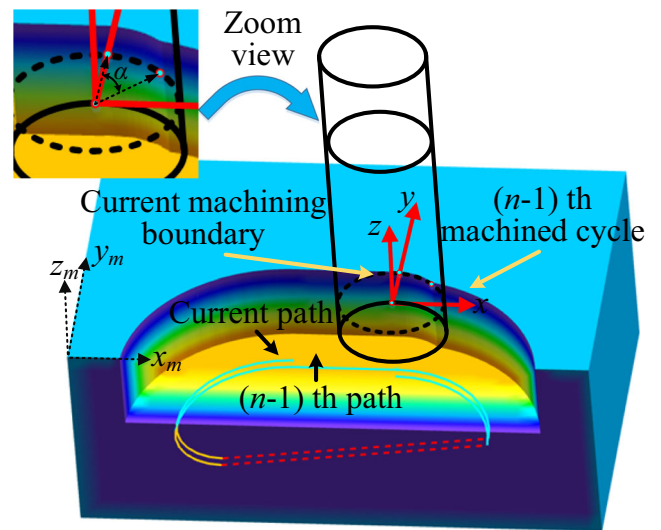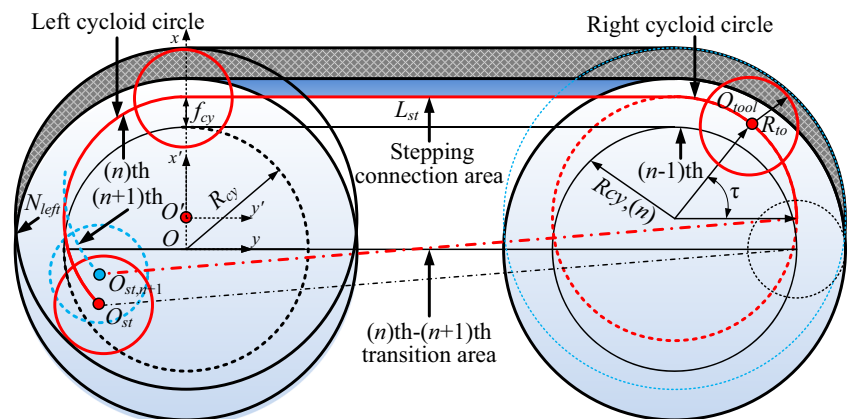
decreases. In the step interval, because the wrap angle remains unchanged, the cycloid position angle remains constant, and the cutting force remains unchanged. The cutting force changes smoothly throughout the cycle. Compared with conventional machining, the range of the maximum cutting force of U-pass milling is reduced by approximately 25%, while the mean cutting force is reduced by approximately 60%. The results in the Fig. 8 show that U-pass milling can effectively reduce the cutting load and improve the local load surge caused by sudden changes in the material removal rate.

3 Tool path planning

3.1 Pretreatment of the milling boundary

The single runner of the integral impeller is taken as the object for the five-axis U-pass milling. For the convenience of subsequent calculations, we define the curve composed of the array of midpoints on the flow channel boundary as the centerline, its starting point is then rotated to the $[YOZ]$ plane of

Fig. 4 U-pass milling tool path

Fig. 6 Milling comparison tests
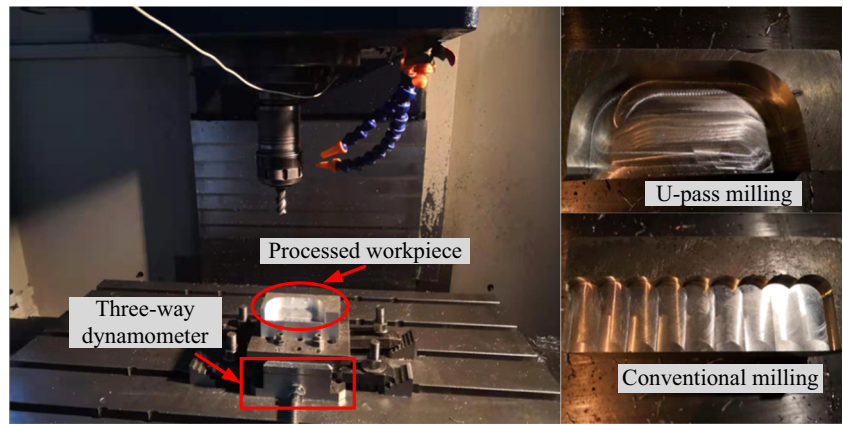
Cartesian coordinate system, and the rotation angle, θ_{ct}, is obtained from the coordinates of the point as shown in Eq. 2. Finally, all of the boundary parameters are converted to a rotation coordinate system according to the conversion matrix.

$$\theta_{ct} = -arc\tan\left(\frac{y_{ct,1}}{x_{ct,1}}\right) \tag{2}$$

where $[x_{cy} \; y_{ct}]$ is the centerline node, $[x_{cy,1} \; y_{ct,1}]$ is the corresponding starting point.

The matrix is as follows:

$$\begin{bmatrix} x_{l,sft} & y_{l,sft} & z_{l,sft} \\ x_{r,sft} & x_{r,sft} & x_{r,sft} \\ x_{c,sft} & x_{c,sft} & x_{c,sft} \end{bmatrix}$$
$$= \begin{bmatrix} x_{lori,sft} & y_{lori,sft} & z_{lori,sft} \\ x_{rori,sft} & x_{rori,sft} & x_{rori,sft} \\ x_{cori,sft} & x_{cori,sft} & x_{cori,sft} \end{bmatrix} * \begin{bmatrix} \cos(\theta_{ct}) & \sin(\theta_{ct}) & 0 \\ -\sin(\theta_{ct}) & \cos(\theta_{ct}) & 0 \\ 0 & 0 & 1 \end{bmatrix} \tag{3}$$

where $[x_{l,sft} \; y_{l,sft} \; z_{l,sft}]$, $[x_{r,sft} \; y_{r,sft} \; z_{r,sft}]$, $[x_{c,sft} \; y_{c,sft} \; z_{c,sft}]$ are the shaft disk surface boundary and centerline nodes after

rotation, $[x_{lori,sft} \; y_{lori,sft} \; z_{lori,sft}]$, $[x_{rori,sft} \; y_{rori,sft} \; z_{rori,sft}]$, $[x_{cori,sft} \; y_{cori,sft} \; z_{cori,sft}]$ are the corresponding original sample nodes.

To avoid a sudden increase in the tool–workpiece wrap angle in the runner inlet, as the occurrence of full-edge cutting can cause a sudden increase in local load and even tool breakage, it is necessary to pretreat the milling boundary. By increasing the sum of the cycloid cycle radius and tool radius along the generatrix direction to extend the boundary, the expanded generatrix is obtained using the interpolation method. The original boundary data points on both sides of the impeller and the expanded bottom circle radius are combined to obtain the analytical value of the end point of the boundary expansion:

$$\begin{cases} y = a_1 x^3 + a_2 x^2 + a_3 x + a_4 \\ x^2 + y^2 = \left(R_{gene} + r_{cyc} + r_{to}\right)^2 \end{cases} \tag{4}$$

where $[x, y]$ is the extended boundary, R_{gene} is the radius of the original impeller, and r_{cyc} and r_{to} are the cycloid cycle radius and tool radius, respectively. The pretreatment result is shown in Fig. 9.

Table 1 Cutting parameters and comparison results

Processing mode	Cutting speed	Feed per tooth	MRR	Cutting depth	Cutting force	Maximum cutting force
	(m/min)	(mm/min)	(cm³/min)	(mm)	(N)	(N)
U Pass	100	0.04	2	20	111.41	528.91
Conventional milling	33.3			5	214.74	657.09
U Pass	147	0.06	2.94	20	132.66	601.72
Conventional milling	49			5	307.68	782.22
U Pass	216	0.09	4.32	20	166.52	698.78
Conventional milling	72.4			5	383.75	855.86
U Pass	279	0.12	5.58	20	195.26	791.69
Conventional milling	93.3			5	471.05	948.69
U Pass	353	0.15	7.06	20	225.76	862.62
Conventional milling	117.6			5	549.54	1102.54

Fig. 7 Milling force distributions

(a)

(b)

(c)

(d)
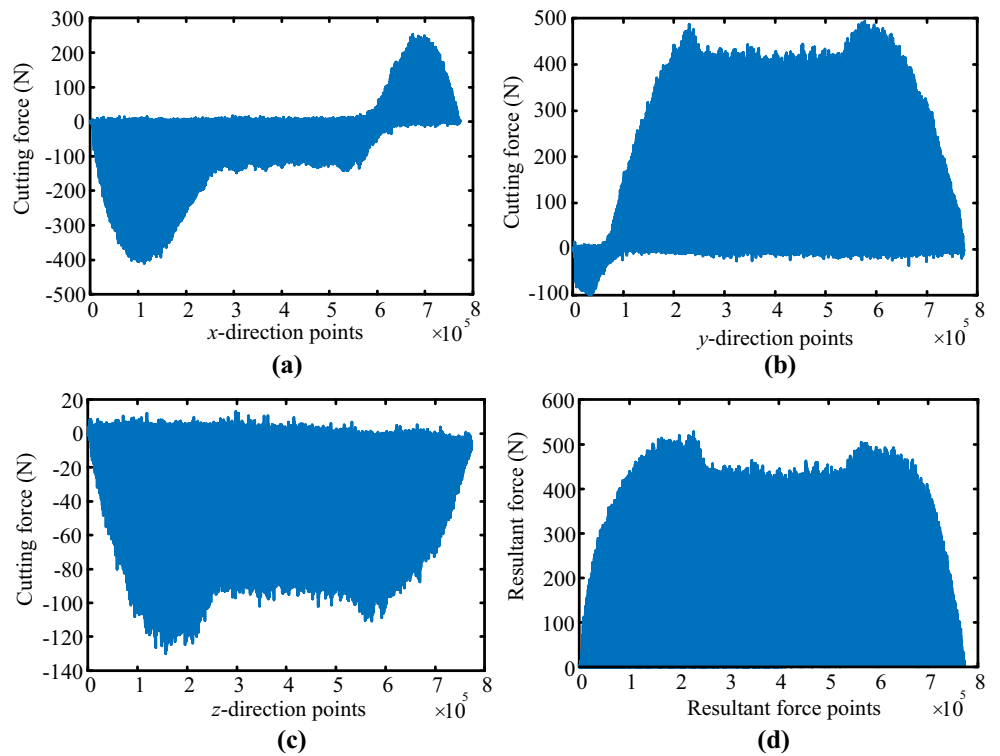
3.2 Mapping model establishment

Considering the complexity of space path construction, a mapping algorithm for tiling micro-arcs is proposed. This algorithm maps the boundary of the three-dimensional geometric domain to the plane of the two-dimensional parameter domain with the arc length as the coordinate axis to realize the dimensionality reduction calculation of the space point set. First, the functional relationship between the section distance and height of the generatrix is established, and the interpolation spline nodes are set as segment points. The segment basis functions are integrated in different intervals, and the $(i-1)$th node and (i)th node are taken as the upper and lower bounds of the integration, respectively. Finally, all of the intervals are

traversed, and the arc length is iterated. The arc length of the first interval is defined as the initial value, and the arc length of the (i)th node is:

$$\begin{cases} Larc_0 = 0; \\ Larc_i = Larc_{i-1} + \int_{p_{down}}^{p_{up}} \sqrt{1 + \left(\dfrac{dcoef_i}{dx}\right)^2}; & i = 1, 2, 3 \cdots, n \end{cases}$$

(5)

where $Larc_i$ is the iterative arc length at the (i)th node, $coef_i$ is the basis function in the current node interval, and p_{up} and p_{down} are the boundaries of the node interval. Finally, the mapping value of the generatrix in the parameter domain is obtained. To reduce the amount of calculation, the boundary
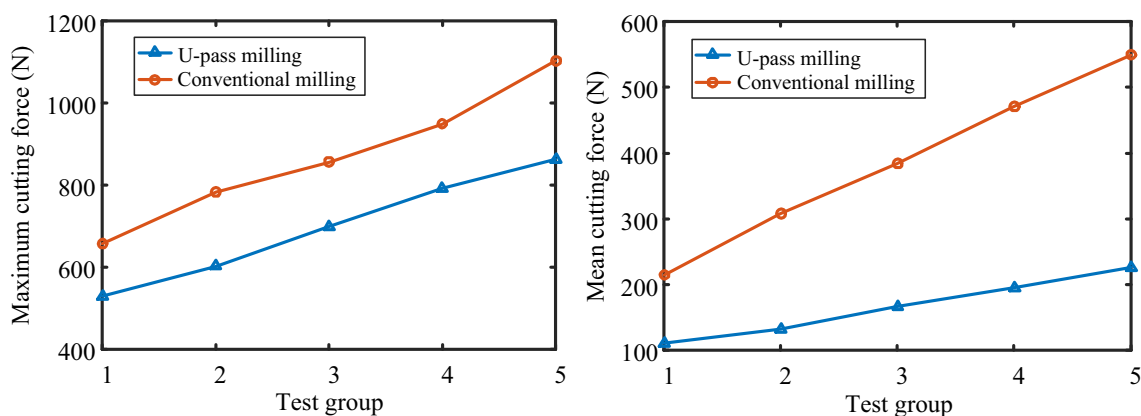
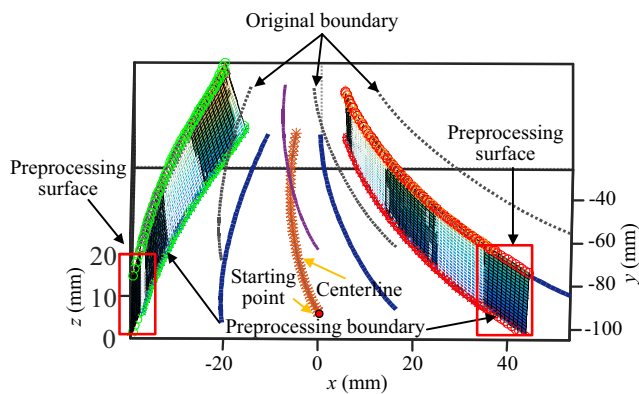

Fig. 8 Milling force comparison

Fig. 9 Boundary preprocessing

Fig. 10 Arc length mapping

node height proportion value is used as the variable parameter of the subsequent calculation, as shown in Eq. 6. If $Z_{rix,end}$ is zero in the actual calculation, an infinitesimal amount must be added:

$$pr_i = \frac{z_{rix,i}}{z_{rix,end}} \tag{6}$$

where pr_i is the height proportion of the (i)th node. The height proportion to arc length function is established and taken as the ordinate of the parameter domain. According to the above method, the arc length of the geometric domain on both sides of the boundary is mapped to the parameter domain coordinate system as the ordinate value in Fig. 10.

The abscissa of the parameter domain mapping is determined by unfolding the arc length of the current cross-section as shown in Fig. 11. The corresponding arc length is calculated according to the section distance and abscissa of the interpolation interval where any point is located, and the starting point of the midline, O_{par}, determined by the two boundaries is defined as the origin of the parameter domain. The calculation results are as follows:

$$x_{par} = \arctan\left(\frac{y_{rb,i}}{x_{rb,i}}\right) f\left(z_{rb,i}\right) \tag{7}$$

where $[x_{rb,i} \; y_{rb,i}]$ are the coordinates of the boundary curve on the geometric domain, t_i, and $f(z_{rb,i})$ is the interpolation function at the (i)th node. If the adjacent coordinates are in the same interval of spline interpolation, the corresponding basis functions are the same.

All of the geometric domain boundary curves are mapped to the parameter domain; the boundary arc length corresponds to the parameter domain mapping ordinate, and the current cross-section expansion arc length corresponds to the parameter domain mapping abscissa. Tool path planning is subsequently performed in the dimensionally reduced coordinate system. The dimensionality reduction results are presented in Fig. 12.
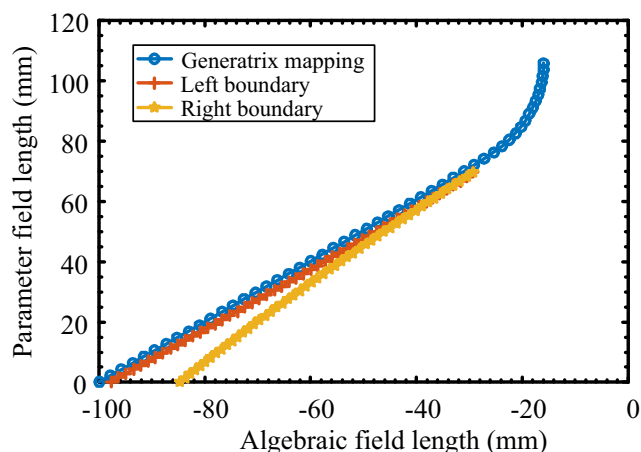
3.3 Tool contact points calculation

Tool path planning includes calculation of the tool position point and tool axis vector. In particular, for milling tools with complex end faces, such as ball-end milling cutters in five-axis machining, the instantaneous tool position point and tool contact point are not the same. Considering the characteristics of the U-pass milling tool path, the calculation methods for the tool contact point in different cycloid areas differ. In the parameter domain, with the runner curve of the dimension reduction mapping as the boundary condition, the analytical contact model of a single-cycle path is established as shown in Fig. 13, and then the entire runner is traversed.

In the left cycloid circle area, the center of the current cycloid circle is calculated based on the slope of the proportional node and the corresponding cycloid circle equation:

$$\begin{cases} (x_1-x_{o1})^2 + (y_1-y_{o1})^2 = (R_{cy} + r_{to})^2 \\ \dfrac{y_1-y_{o1}}{x_1-x_{o1}} = -\dfrac{1}{\displaystyle\sum_{i=0}^{n-1} N_{i+1,p-1}(u)\dfrac{p}{u_{i+p+1}-u_{i+1}}(P_{i+1}-P_i)} \end{cases} \tag{8}$$

where the proportional node, Q, is $[x_1 \; y_1]$, and $[x_{o1} \; y_{o1}]$ is the corresponding cycloid circle center, O_1. The cubic spline function is selected for interpolation, $p = 3$, and P is the control vertex of the spline curve.

As described above, the calculation for the right cycloid cycle area is as follows:

$$\begin{cases} (x_{r1}-x_{or1})^2 + (y_{r1}-y_{or1})^2 = (R_{cy} + r_{to})^2 \\ \dfrac{y_{r1}-y_{or1}}{x_{r1}-x_{or1}} = -\dfrac{1}{\displaystyle\sum_{i=0}^{n-1} N^r_{i+1,p-1}(u)\dfrac{p^r}{u_{i+p+1}-u_{i+1}}(P^r_{i+1}-P^r_i)} \end{cases} \tag{9}$$

where the proportional node, Q, is $[x_{r1} \; y_{r1}]$, and $[x_{or1} \; y_{or1}]$ is the corresponding cycloid circle center, O_{r1}.

The direction vectors of the step connecting line, L_{st}, and the connecting line vector of the center of the cycloid circle on

Fig. 11 Cross-section arc length calculation
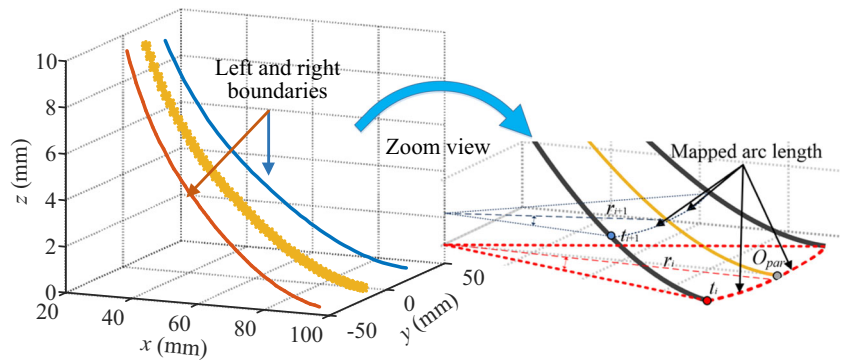
both sides are calculated, and analytical equations are established with the left and right cycloid circles as the boundary conditions:

$$
\begin{cases}
\dfrac{y_{f1}-y_{o1}}{x_{f1}-x_{o1}} = -\dfrac{x_{or1}-x_{o1}}{y_{or1}-y_{o1}} \\
\left(x_{f1}-x_{o1}\right)^2 + \left(y_{f1}-y_{o1}\right)^2 = R_{cy}^{\ 2} \\
\dfrac{y_{rf1}-y_{or1}}{x_{rf1}-x_{or1}} = -\dfrac{x_{or1}-x_{o1}}{y_{or1}-y_{o1}} \\
\left(x_{rf1}-x_{ro1}\right)^2 + \left(y_{rf1}-y_{ro1}\right)^2 = R_{cy}^{\ 2}
\end{cases}
\tag{10}
$$

where $[x_f\, y_f]$ is the starting point coordinate of the left cycloid cycle stepping connection line, Q_{tr}, and $[x_{rf}\, y_{rf}]$ is the right cycloid circular stepping connection line ending point coordinates, M_{tr}.

Considering the actual processing requirements, to ensure that the last cycle of the tool just reaches the boundary end position, it is necessary to calculate whether the current processing path exceeds the end position at the beginning of each cycloid cycle. This is used as the criterion to search for the path end point:

$$
\begin{cases}
y_{oend} \geq y_{end} - r_{to} - R_{cy} \\
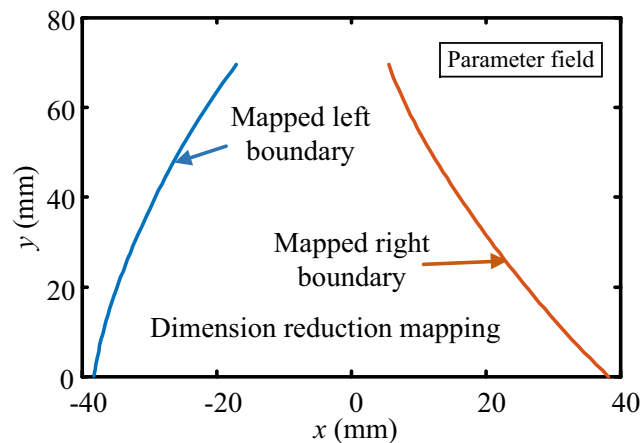y_{loend} \geq y_{rend} - r_{to} - R_{cy}
\end{cases}
\tag{11}
$$

where y_{end} and y_{rend} are the end of the left and right boundaries of the parameter domain, respectively. By combining the above algorithm to traverse the tool contact point in the entire cycle, as shown in Fig. 14, the tool path distribution form of the entire parameter domain dimension reduction mapping is finally obtained.

According to the tool connection point of the parameter domain, the ordinate under the parameter domain is converted to a three-dimensional geometric domain through the above-mentioned interpolation function, and the cross-section distance of the corresponding position is obtained by inverse calculation of the cross-section arc length. The coordinate points of the $[XOY]$ plane of the geometric domain can be obtained using the cross-section distance:

$$
\begin{cases}
x_{al} = r_{al}\sin\left(\dfrac{x_{par}}{r_{al}}\right) \\
y_{al} = r_{al}\cos\left(\dfrac{x_{par}}{r_{al}}\right)
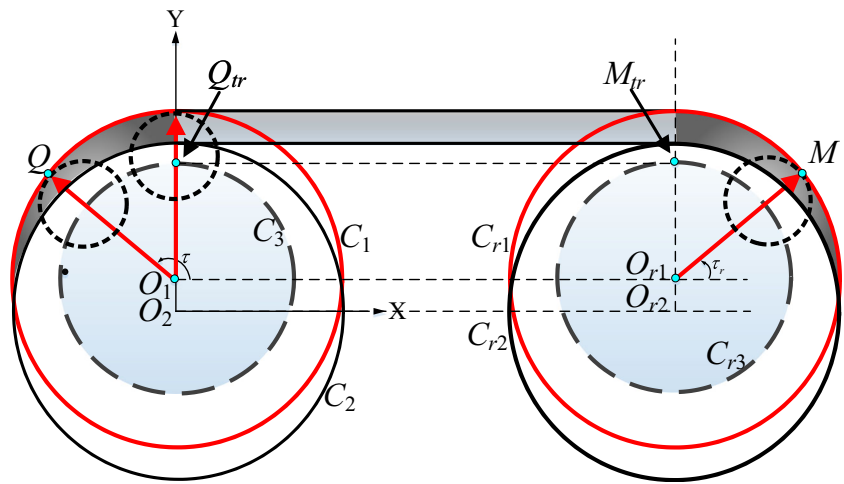\end{cases}
\tag{12}
$$

where x_{pra} and r_{al} are the abscissa of the parameter domain and the cross-sectional distance of the geometric domain, respectively. Finally, by integrating the tool contact point, a five-axis U-pass milling tool contact point distribution form can be obtained as shown in Fig. 15.

3.4 Bidirectional proportional domain calculation

Tool interference is a problem that cannot be ignored in impeller machining. When interference occurs, it can easily cause workpiece damage, tool breakage, or even machine tool breakdown. In this study, focusing on the problem of U-pass milling tool axis vector planning, a bidirectional proportional domain mapping algorithm is established to realize interference-free five-axis U-pass milling tool axis vector planning.

First, the least squares method is used to obtain the transfer functions of the double-axis coordinates of the shaft disk surface with respect to the proportional node. Four multivariate functions can be obtained by fitting; to ensure calculation

Fig. 12 Dimension reduction mapping in the parameter domain

Fig. 13 Tool contact point calculation

accuracy and efficiency, the sixth-order function fitting is selected here.

$$\begin{cases} \left[\Phi_x^{L1}(L_1 rat), \Phi_y^{L1}(L_1 rat) \right] \\ \left[\Phi_x^{L2}(L_2 rat), \Phi_y^{L2}(L_2 rat) \right] \end{cases} \tag{13}$$

where $\Phi L1\ x(L_1 rat)$ and $\Phi L1\ y(L_1 rat)$ are the fitting functions at the proportional nodes of the left spline boundary curve, and $\Phi L2\ x(L_2 rat)$ and $\Phi L2\ y(L_2 rat)$ are the fitting functions corresponding to the right spline boundary curve.

According to the parameter equation:

$$S(i,j) = (1-v)p(u) + vg(u) \tag{14}$$

The proportional function and the obtained instantaneous tool contact point $[x_{ins}\ y_{ins}]$ are introduced, and the proportional coordinates $[u_i\ v_i]$ of this point are calculated. The calculation results are as follows:

$$\begin{cases} x_{ins} = (1-v_i)\Phi_x^{L1}(u_i) + v_i\Phi_x^{L2}(u_i) \\ y_{ins} = (1-v_i)\Phi_y^{L1}(u_i) + v_i\Phi_y^{L2}(u_i) \end{cases} \tag{15}$$

The obtained $[u_i\ v_i]$ is the instantaneous bidirectional proportional parameter of the tool contact point, $[x_{ins}\ y_{ins}]$. According to the above method, all cycloid cycle tool contact points are traversed to obtain the complete tool path bidirectional proportional domain.

3.5 U-pass milling tool path

A bidirectional proportional domain model of the cover surface is established according to the bidirectional proportional domain algorithm above with the given cover disk surface parameters as boundary conditions. Based on the proportion of the tool contact point obtained in the previous section, the same proportional point on the cover surface can be searched in reverse. The reverse operation is given by Eq. (16).
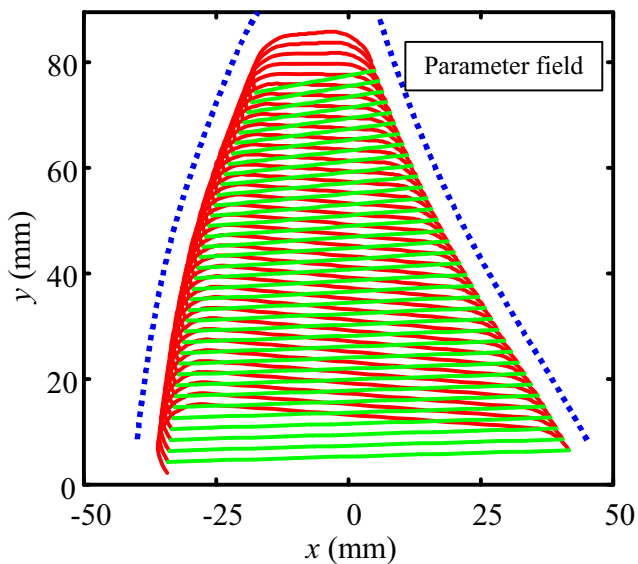

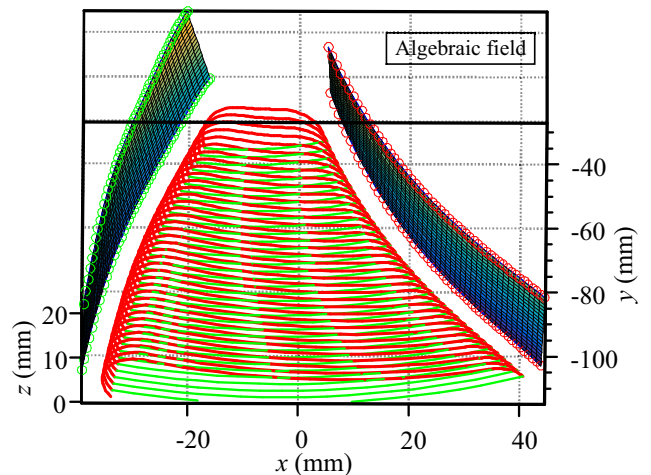Fig. 14 Distribution of tool contact points

Fig. 15 Tool contact points in the geometric domain

$$\begin{cases} x_i^{co} = (1-v_i)\chi_x^{L1}(u_i) + v_i\chi_x^{L2}(u_i) \\ y_i^{co} = (1-v_i)\chi_y^{L1}(u_i) + v_i\chi_y^{L2}(u_i) \end{cases} \quad (16)$$

where $[x_{co\ i}\ y_{co\ i}]$ is the proportional coordinates of the cover disk surface, and $\chi_{L1}\ x(u_i)$, $\chi_{L2}\ x(u_i)$, $\chi_{L1}\ y(u_i)$, and $\chi_{L2}\ y(u_i)$ are the transfer functions of the proportional nodes of the cover disk surface with respect to the double-axis coordinates.

The instantaneous proportional points of the cover disk surface and the shaft disk surface are denoted as $O_{co\ ins}$ and $O_{st\ ins}$, respectively. Connecting two equal-proportion points and unitizing the vector yields Eq. (17).

$$e_{ins} = \frac{\bar{l}_{ins}}{|\bar{l}_{ins}|} = \frac{x_i^{co}-x_{ins}}{\|O_{ins}^{co}-O_{ins}^{st}\|}i + \frac{y_i^{co}-y_{ins}}{\|O_{ins}^{co}-O_{ins}^{st}\|}j + \frac{z_i^{co}-z_{ins}}{\|O_{ins}^{co}-O_{ins}^{st}\|}k \quad (17)$$

Considering that the tool position point of ball-end milling is different from the tool contact point in the actual machining, the APT programming language needs to be embedded in the corresponding tool position point instead of the tool contact point. First, the tool contact point, T_{con}, is moved along the normal vector of the current surface micro-element by the length of the radius of the ball head, i.e., the position of the ball center corresponding to the current tool contact, TO_{cen}. Then, the current tool position point, T_{pos}, can be solved in the radius range with the center of the ball as the origin according to the equation of circle parameters and corresponding vector, as shown in Fig. 16.

To facilitate the calculation of the position of the center point of the sphere, an inverse mapping method on the space vector is established, and the corresponding position vector in the three-dimensional space is obtained through the inverse calculation of any initial vector in the parameter domain. The inverse operation calculation is shown in Fig. 17.

According to the spline interpolation function, a series of nodal derivative functions are obtained by deriving the spline basis function segment-by-segment in Eq. 18. The first point value is brought into the range of the initial end derivative
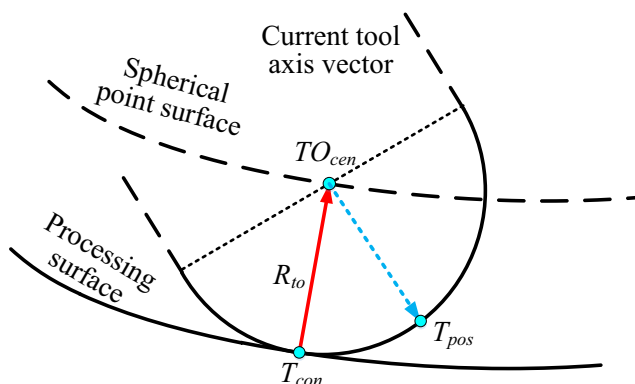

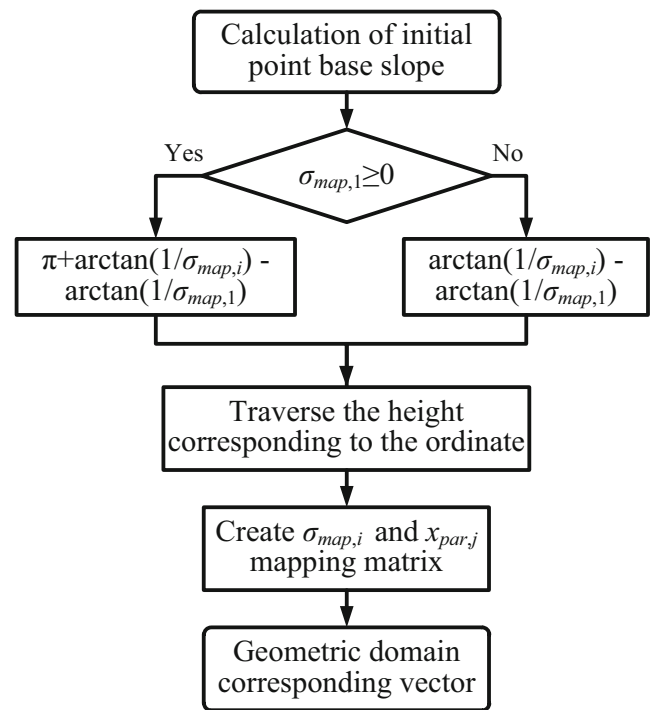**Fig. 16** Calculation of tool position points

Fig. 17 Parameter domain vector mapping

function, and the calculated result of the point is defined as the node base slope.

$$\frac{dy_{map,i}}{dx_{map,i}} = \sum_{i=0}^{n-1} N_{i+1,p-1}^{map}(z) \frac{p^{map}}{z_{i+p+1}-z_{i+1}}\left(p^{map}_{i+1}-p^{map}_i\right) \quad (18)$$

The difference between the derivative of each node and the base slope is calculated to obtain the offset angle of each node. The parameter domain vector is subjected to two matrix iterations according to the current offset angle and the node base slope. Then, through the initial origin matrix conversion in Eq. 19, the corresponding vector in three-dimensional space is obtained.

$$[i_{al,i}\ j_{al,i}\ k_{al,i}] = [i_{par}\ j_{par}\ k_{par}] * \begin{bmatrix} \cos(\sigma_{map,1}) & 0 & \sin(\sigma_{map,1}) \\ 0 & 1 & 0 \\ -\sin(\sigma_{map,1}) & 0 & \cos(\sigma_{map,1}) \end{bmatrix}$$
$$* \begin{bmatrix} \cos(\sigma_{map,i}) & 0 & -\sin(\sigma_{map,i}) \\ 0 & 1 & 0 \\ \sin(\sigma_{map,i}) & 0 & \cos(\sigma_{map,i}) \end{bmatrix} * \begin{bmatrix} \cos\left(\frac{x_{par,j}}{r_{par,j}}\right) & -\sin\left(\frac{x_{par,j}}{r_{par,j}}\right) & 0 \\ \sin\left(\frac{x_{par,j}}{r_{par,j}}\right) & \cos\left(\frac{x_{par,j}}{r_{par,j}}\right) & 0 \\ 0 & 0 & 1 \end{bmatrix}$$
$$(19)$$

where $[x_{par}\ y_{par}\ z_{par}]$ is the parameter domain tool contact point, $dy_{map,i}/dx_{map,i}$ is the derivative of the (i)th node of the parameter domain, $[i_{al,i}\ j_{al,i}\ k_{al,i}]$ and $[i_{par}\ j_{par}\ k_{par}]$ are the geometric domain mapping vector and parameter domain vector, respectively, and $\sigma_{map,1}$ and $\sigma_{map,i}$ are the initial point and subsequent node offset angles of the parameter domain, respectively.

Finally, using the above algorithm, the U-pass milling tool path is obtained, and the single path is shown in Fig. 18.

Fig. 18 Single-cycle tool path
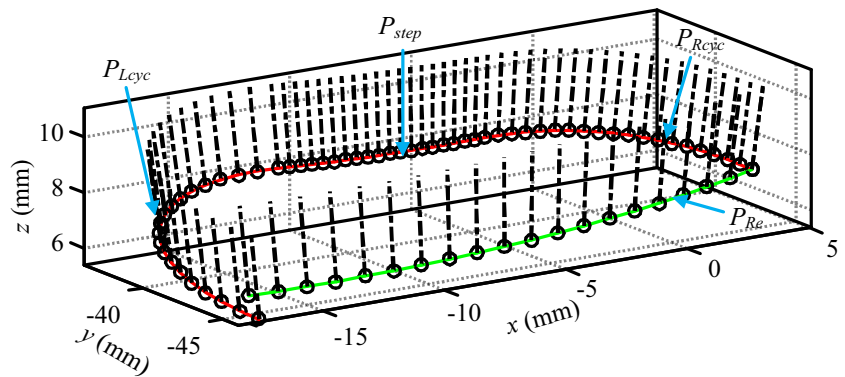
4 Example verification

The feasibility of the path is verified using a numerical example. To adapt to the reading methods of different machine tools, the tool path is directly programmed in the form of the APT language. As the underlying code of the machine tool, the APT language can be directly adapted into a formal code through post-processing. In Fig. 18, P_{Lcyc} and P_{Rcyc} contain two cutting areas, with a total of $2T$ tool position points with $T = 10$; here, P_{step} is located in a larger stepping area, so the number of tool position points is set to $3T$. the U-pass milling tool position points and tool axis vectors are embedded in the APT language code string, and the entire code string is post-processed to obtain the corresponding machine tool language.

Finally, by configuring the processing module, it is verified that the tool path is effective as shown in Fig. 19. It can be seen that not only the ball head, but also part of the side edge of the tool participates in the cutting, which avoids the load concentration caused by the tool tip as the main cutting area. In each rotation cycle, the wrap angle is small, and the tool is not always in the cutting state during a single cycloid cycle. Thus, there is sufficient cooling time to effectively discharge the cutting heat, reduce the cutting temperature, and greatly improve the tool life.
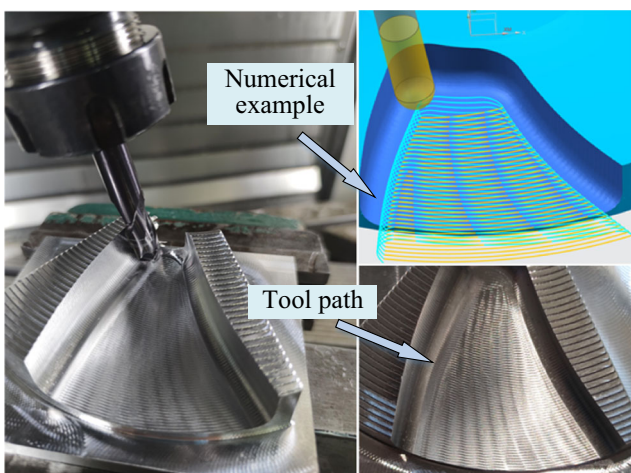

Fig. 19 Numerical example and milling test

5 Conclusion

(1). A geometric model of U-pass milling is established, and the characterization parameters of the path are defined. Through comparative tests of three-axis groove milling, it is demonstrated that the peak value and average value of the cutting force are reduced by 25% and 60%, respectively.

(2). Taking the impeller runner as the processing object, pretreatment of the milling boundary parameters is performed. A mapping algorithm for tiling micro-arcs is proposed. The three-dimensional boundary is mapped to the two-dimensional parametric domain plane with the arc length as the coordinate axis through piecewise integration and arc length iteration. Considering the different contact conditions of the tool in different cycloid areas, an analytical model of the tool contact point is established in the left and right cycloid circle areas and the step connection area.

(3). The bidirectional proportional domain algorithm is established, and then the equal-proportional positions of shaft disk surface and cover disk surface are obtained; Based on the piecewise derivation of the basis function and multiple matrix transformation, the vector of the parameter field is inversely mapped, and then the coordinates of the current tool position are solved by the tool contact point and corresponding vector. Finally, the interference-free U-pass milling tool axis vector planning is realized. The tool position points and tool axis vectors are embedded in the APT code string, and the feasibility of this five-axis U-pass milling tool path planning method is verified through a numerical example and the corresponding milling test.

Declarations

Ethics approval Not applicable.

Consent to participate Not applicable.

Consent to publication Not applicable.

Competing interests The authors declare no competing interests.

References

1. Fan HZ, Xi G, Wang W, Cao YL (2016) An efficient five-axis machining method of centrifugal impeller based on regional milling. Int J Adv Manuf Technol 87(1-4):789–799. https://doi.org/10.1007/s00170-016-8467-x

2. Chu CH, Huang WN, Li YW (2012) An integrated framework of tool path planning in 5-axis machining of centrifugal impeller with split blades. J Intell Manuf 23(3):687–698. https://doi.org/10.1007/s10845-010-0419-y

3. Lee YS, Koc B (1998) Ellipse-offset approach and inclined zig-zag method for multi-axis roughing of ruled surface pockets. Comput Aided Des 30(12):957–971. https://doi.org/10.1016/S0010-4485(98)00051-7

4. Alberro AN, Rojas HG, Egea AS, Hameed S, Aguilar RP (2019) Model Based on an Effective Material-Removal Rate to Evaluate Specific Energy Consumption in Grinding. Materials 12(6):939. https://doi.org/10.3390/ma12060939

5. Heo EY, Kim DW, Kim BH, Jang DK, Chen FF (2008) Efficient rough-cut plan for machining an impeller with a 5-axis NC machine. Int J Comput Integr Manuf 21(8):971–983. https://doi.org/10.1080/09511920802010761

6. Elber G, Cohen E (1994) Tool path generation for freeform surface models. Comput Aided Des 26(6):490–496. https://doi.org/10.1145/164360.164500

7. Kim BH, Choi BK (2000) Guide surface based tool path generation in 3-axis milling: an extension of the guide plane method. Comput Aided Des 32(3):191–199. https://doi.org/10.1016/S0010-4485(99)00086-X

8. Lee SG, Kim HC, Yang MY (2008) Mesh-based tool path generation for constant scallop-height machining. Int J Adv Manuf Technol 37(1-2):15–22. https://doi.org/10.1007/s00170-007-0943-x

9. Huang N, Krebs E, Baumann J, Zhou Y, Biermann D (2020) Experimental investigation on influence of engagement angle and tool geometry on plunge milling. Int J Adv Manuf Technol 108(1-4):1973–1981. https://doi.org/10.1007/s00170-020-05480-x

10. Montassar F, Frédéric M, Johanna S, Walter R (2021) Cutting parameters and tool geometry selection for plunge milling - Analysis of cutting forces at the bottom of deep titanium workpieces. J Manuf Process 62:491–500. https://doi.org/10.1016/J.JMAPRO.2020.12.033

11. Gao HN, Shen HD, Liu XL, Li RY (2020) Mechanics and dynamics research considering the tool radial runout effect in plunge milling. Int J Adv Manuf Technol 106(9–12):2391–2402. https://doi.org/10.1007/s00170-019-04780-1

12. Wakaoka S, Yamane Y, Sekiya K, Narutaki N (2002) High-speed and high-accuracy plunge cutting for vertical walls. J Mater Process Technol 127(2):246–250. https://doi.org/10.1016/S0924-0136(02)00151-6

13. Cafieri S, Monies F, Mongeau M, Bes C (2016) Plunge milling time optimization via mixed-integer nonlinear programming. Comput Ind Eng 98(8):434–445. https://doi.org/10.1016/j.cie.2016.06.015

14. Danis I, Wojtowicz N, Monies F, Lamesle P, Lagarrigue P (2013) Cutting Conditions and Surface Integrity During Dry Plunge-milling of a Wrought Magnesium Alloy. Procedia Eng 63(1):36–44. https://doi.org/10.1016/j.proeng.2013.08.213

15. Rauch M, Hascoet JY (2012) Selecting a milling strategy with regard to the machine tool capabilities: application to plunge milling. Int J Adv Manuf Technol 59(1-4):47–54. https://doi.org/10.1007/s00170-011-3498-9

16. Chu CH, Chen HY, Chang CH (2020) Continuity-preserving tool path generation for minimizing machining errors in five-axis CNC flank milling of ruled surfaces. J Manuf Syst 55:171–178. https://doi.org/10.1016/j.jmsy.2020.03.004

17. Chu CH, Wu PH, Lei W (2012) Tool path planning for 5-axis flank milling of ruled surfaces considering CNC linear interpolation. J Intell Manuf 23(3):471–480. https://doi.org/10.1007/s10845-010-0386-3

18. Lu YA, Wang CY (2020) Smoothing method of generating flank milling tool paths for five-axis flat-end machining considering constraints. Int J Adv Manuf Technol 110(11-12):3295–3309. https://doi.org/10.1007/s00170-020-05880-z

19. Lu YA, Wang CY, Zhou L (2019) Geometric deviation evaluation for a five-axis flank milling tool path using the tool swept envelope. Int J Adv Manuf Technol 105(10):1811–1821. https://doi.org/10.1007/s00170-019-04397-4

20. Chaves-Jacob J, Poulachon G, Duc E (2012) Optimal strategy for finishing impeller blades using 5-axis machining. Int J Adv Manuf Technol 58(5):573–583. https://doi.org/10.1007/s00170-011-3424-1

21. Elber G, Cohen E, Drake S (2004) MATHSM: medial axis transform toward high speed machining of pockets. Comput Aided Des 37(2):241–250. https://doi.org/10.1016/j.cad.2004.05.008

22. Rauch M, Duc E, Hascoet JY (2008) Improving trochoidal tool paths generation and implementation using process constraints modelling. Int J Mach Tools Manuf 49(5):375–383. https://doi.org/10.1016/j.ijmachtools.2008.12.006

23. Ibaraki S, Yamaji I, Matsubara A (2010) On the removal of critical cutting regions by trochoidal grooving. Precis Eng 34(3):467–473. https://doi.org/10.1016/j.precisioneng.2010.01.007

24. Santhakumar J, Iqbal UM (2019) Role of trochoidal machining process parameter and chip morphology studies during end milling of AISI D3 steel. J Intell Manuf 32(3):649–665. https://doi.org/10.1007/S10845-019-01517-5

25. Niaki FA, Pleta A, Mears L (2018) Trochoidal milling: investigation of a new approach on uncut chip thickness modeling and cutting force simulation in an alternative path planning strategy. Int J Adv Manuf Technol 97(1):641–656. https://doi.org/10.1007/s00170-018-1967-0

26. Ajgalík M, Kunerová M, Harniárová M, Valíek J, Kmec J (2020) Analysis and Prediction of the Machining Force Depending on the Parameters of Trochoidal Milling of Hardened Steel. Appl Sci 10(5):1788. https://doi.org/10.3390/app10051788

27. Luo M, Hah C, Hafeez HH (2019) Four-axis trochoidal toolpath planning for rough milling of aero-engine blisks. Chin J Aeronaut 32(8):217–224. https://doi.org/10.1016/j.cja.2018.09.001

28. Pleta A, Niaki FA, Mears L (2017) Investigation of Chip Thickness and Force Modelling of Trochoidal Milling. Procedia Manuf 10: 612–621. https://doi.org/10.1016/j.promfg.2017.07.063

29. Waszczuk K, Karolczak P, Wisniewska M, Kowalski M (2017) Influence of the path type on selected technological effects in the trochoidal milling. Adv Sci Technol Res J 11(1):147–153. https://doi.org/10.12913/22998624/66501

30. Oh NS, Woo WS, Lee CM (2018) A study on the machining characteristics and energy efficiency of Ti-6Al-4V in laser-assisted trochoidal milling. Int J Precis Eng Manuf-Green Technol 5(1):37–45. https://doi.org/10.1007/s40684-018-0004-y

Publisher's note Springer Nature remains neutral with regard to jurisdictional claims in published maps and institutional affiliations.